Thin Solid Films 520 (2012) 2316–2320

Contents lists available at SciVerse ScienceDirect

Thin Solid Films

journal homepage: www.elsevier.com/locate/tsf

Crystallization behavior and mechanical properties of erbium oxide coatings fabricated by pulsed magnetron sputtering

Xinlian Li, Ping Wu *, Hong Qiu, Sen Chen, Binbin Song

Department of Physics, School of Applied Science, University of Science and Technology Beijing, 30 Xueyuan Road, Haidian District, Beijing 100083, China

ARTICLE INFO

Article history:
Received 16 July 2010
Received in revised form 31 August 2011
Accepted 16 September 2011
Available online 29 September 2011

Keywords:
Erbium oxide
Monoclinic
Pulsed magnetron sputtering
Annealing
Hardness
Elastic modulus

ABSTRACT

Erbium oxide coatings were prepared by mid-frequency pulsed magnetron sputtering at different sputtering powers and substrate temperatures. Atomic force microscopy, X-ray photoelectron spectroscopy, X-ray diffraction, and nanoindentation were used to investigate surface morphologies, compositions, crystallization behavior, and mechanical properties of the coatings, respectively. The thermal stability of the coating structure was also investigated. A monoclinic phase was observed in the erbium oxide coatings prepared at substrate temperatures below 350 °C. A cubic phase was obtained by elevating the temperature to 500 °C. The monoclinic phase coatings deposited at elevated substrate temperatures showed high phase stability. The coatings with a cubic phase exhibited higher hardness and elastic modulus than those with a monoclinic phase, attributable to a narrower bond length distribution and a shorter average bond length.

1. Introduction

The properties of Er_2O_3 films have recently been investigated for various applications. An Er_2O_3 thin film with a high dielectric constant is an attractive replacement material for SiO_2 in manufacturing gate dielectrics [1,2]. Optoelectronic applications of Er_2O_3 films have also been investigated [3]. Numerous investigations and tests on Er_2O_3 coatings have revealed the potential application of these materials as tritium diffusion barriers and corrosion-resistant electrical insulation layers [4,5].

To obtain Er_2O_3 films with desired properties, the crystalline structure of Er_2O_3 must be examined. Er_2O_3 generally exists in three different forms, designated as C, B, and H. The cubic C-Er_2O_3 phase is the most stable structure over a wide temperature range at ambient pressure. The metastable monoclinic B-Er_2O_3 and the hexagonal H-Er_2O_3 phases can be obtained at high temperatures [6]. The H-Er_2O_3 phase exists at temperatures near the melting point and disappears when quenched to room temperature (RT) [7]. Studies have shown that pressure [8] and ion irradiation [6] can induce phase transformation from C-Er_2O_3 to B-Er_2O_3. Most studies on Er_2O_3 focused on bulk materials. However, the microstructures of Er_2O_3 films are still insufficiently elucidated. For Er_2O_3 films, the C-Er_2O_3 phase was mostly reported in the literature. The formation of B-Er_2O_3 phase coatings prepared by filtered cathodic arc deposition was also reported by Adelhelm et al. [9]. Additionally, some unidentified crystalline structures have been discovered [4,10]. Further research is necessary to obtain more information on the structures of the Er_2O_3 coating.

The pulsed magnetron sputtering (PMS) has been considered as the optimal method among several processes used for the deposition of insulation coatings for many applications [11,12]. The current study focused on the crystallization behavior of erbium oxide coatings prepared by PMS under different deposition conditions and annealing processes. The influence of the crystallographic phase on the elastic modulus and on the microhardness of the coatings was also discussed.

2. Experimental details

A mid-frequency (40 kHz) asymmetric bipolar PMS device was employed in fabricating erbium oxide coatings. An erbium target (99.9 wt.%) with a diameter of 50 mm was used. The China low activation martensitic steel, designed for fusion power reactors [13], was used as substrate. The dimensions of the substrates were 12 mm × 6 mm × 0.6 mm. The substrates were mirror-polished and cleaned in a multistage ultrasonic cleaning bath with acetone, deionized water, and alcohol. The distance between the substrate and the target was 60 mm. After the chamber was evacuated to a pressure lower than 3×10^{-4} Pa, a gaseous mixture of O_2 and Ar, with a mass flow ratio of 1/30, was introduced into the chamber. Er atoms/ions were sputtered from the erbium metal target and piled up on the substrates in the presence of O_2 to form erbium oxide coatings. The first group of coatings approximately 1 μm thick, was fabricated at sputtering powers of 55, 84, 108, and 132 W while the temperature was fixed at RT. The second group of coatings

* Corresponding author. Tel.: +86 10 62332636; fax: +86 10 62332587.
E-mail address: pingwu@sas.ustb.edu.cn (P. Wu).

0040-6090/$ – see front matter © 2011 Elsevier B.V. All rights reserved.
doi:10.1016/j.tsf.2011.09.053

approximately 1 μm thick, was deposited at substrate temperatures of 200, 350, and 500 °C using a fixed sputtering power of 108 W. After deposition, both groups of coating were placed in a tubular furnace and annealed under Ar atmosphere for 2 h. Two annealing temperatures, 500 and 700 °C, were used.

X-ray photoelectron spectroscopy (XPS) measurements were performed using a PHI Quantera SXM spectrometer with a 45° take-off angle using monochromatic Al Kα radiation (1486.6 eV) after sputtering off the coating surface for 60 s by Ar^+ at 2 keV and 20 mA. The XPS spectra were corrected for charging effects by setting the C 1 s peak for adventitious carbon at 284.8 eV and then shifting the entire spectrum correspondingly. The XPS data was analyzed using the XPSPeak 4.1 program [14]. Gaussian–Lorentzian line shapes with a ratio of 80:20 were used for deconvolution of the spectra after a standard Shirley background subtraction. X-ray diffraction (XRD) was performed using Rigaku D/max-RB diffractometer employing Cu Kα radiation with a wavelength of 0.15417 nm. The X-ray source was operated at a power of 40 kV × 200 mA. The scan speed was 0.1°/s, and the scan step was 0.02°. A Benyuan CSPM 5000 atomic force microscope (AFM) was employed to observe the surface morphologies of the coatings. The AFM was operated in contact mode with a feedback system maintaining a constant contact force of less than 0.2 N/m between the tip and the sample. Nanoindentation tests were performed at RT using an MTS nanoindenter dynamic contact module system. A Berkovich diamond indenter with a half-tip angle of 65.35° was continuously driven into the flat surface of the specimen, with the maximum applied load set at 19 mN.

3. Results and discussions

3.1. As-deposited coatings

The XPS spectra obtained from the bulk of the coatings revealed that only O and Er were present in the bulk material. Fig. 1 illustrates the core level spectra of O 1s and Er 4d of the erbium oxide coating fabricated at 108 W and RT. From Fig. 1a, the O 1s spectrum is composed of two components, labeled as φ and ψ. The low binding energy component ψ at 528.9 eV corresponds to Er_2O_3, whereas the high binding energy component φ at 531.0 eV corresponds to $Er(OH)_3$[3]. The hydroxide may have formed because the coating is highly reactive with ambient water stream [15]. Er 4d (Fig. 1b) consists of a broad peak centered at approximately 167.6 eV that corresponds to Er_2O_3. A similar Er 4d pattern was also observed by Singh et al. [16]. The O/Er ratio of the coating estimated from the areas of O 1s and Er 4d peaks was 1.55, close to the stoichiometric ratio.

The XRD patterns of B-Er_2O_3 were simulated using the program Powdercell [17] using the lattice parameters and atom positions reported in the literature [8,18,19]. Nonsignificant differences were observed in the resultant diffraction peak positions. Guo et al. [8] calculated and optimized the lattice parameters and the atom positions of B-Er_2O_3 and C-Er_2O_3 using ab initio method. In the current paper, the simulated XRD patterns using the data from the study of Guo et al. were used to analyze the coating structure.

Fig. 2 shows the XRD patterns of the Er_2O_3 coatings deposited at sputtering powers of 55, 84, 108, and 132 W. The simulated patterns of B-Er_2O_3 and C-Er_2O_3 are illustrated at the bottom of Fig. 2. Comparisons between the measured and simulated patterns indicate that the XRD peaks centering at approximately 26.4° and 54.5° corresponded to B-Er_2O_3(202) and B-Er_2O_3(−7−12), respectively. The measured positions of both peaks shifted by approximately 0.25° toward a low-angle direction compared with the simulated B-Er_2O_3 pattern. Fig. 2 also shows that two broad diffraction peaks appear at approximately 29.4° and 48.1°. For the XRD pattern associated with the 84 W sputtering power, the broad diffraction peaks centering at approximately 29.4° were well fitted with three Gaussian peaks, denoted as α, β, and γ, as shown in the inset of Fig. 2. These peaks were identified as B-Er_2O_3(111), B-Er_2O_3(401), and B-Er_2O_3(−402), respectively. Compared with the simulated B-Er_2O_3 pattern, the positions of α, β, and γ shifted toward low-angle directions by 0.25°, 0.23°, and 0.25°, respectively. No obvious trace of C-Er_2O_3(222) was detected. However, due to the coincidence of the B-Er_2O_3(313) and C-Er_2O_3(440) peaks, whether C-Er_2O_3(440) contributed to the broad diffraction peaks centering at approximately 48.1° remains unknown. Nevertheless, the XRD results clearly indicate the formation of the B-Er_2O_3 phase in the coatings.

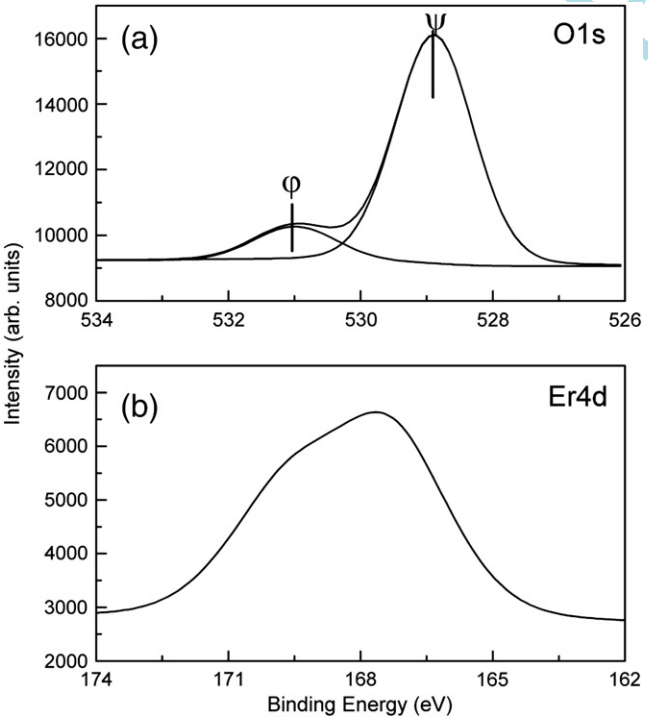

Fig. 1. XPS spectra of (a) O 1s and (b) Er 4d for the erbium oxide coating fabricated at 108 W and RT.

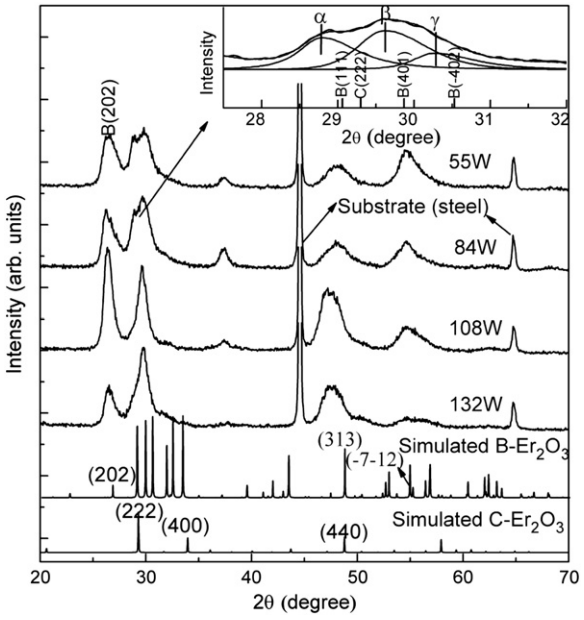

Fig. 2. XRD patterns of Er_2O_3 coatings deposited at various powers at RT. Simulated patterns of B-Er_2O_3 and C-Er_2O_3 are illustrated at the bottom. The inset shows the fitting of the peak between 27.5° and 32.0° for the coating deposited at 84 W.

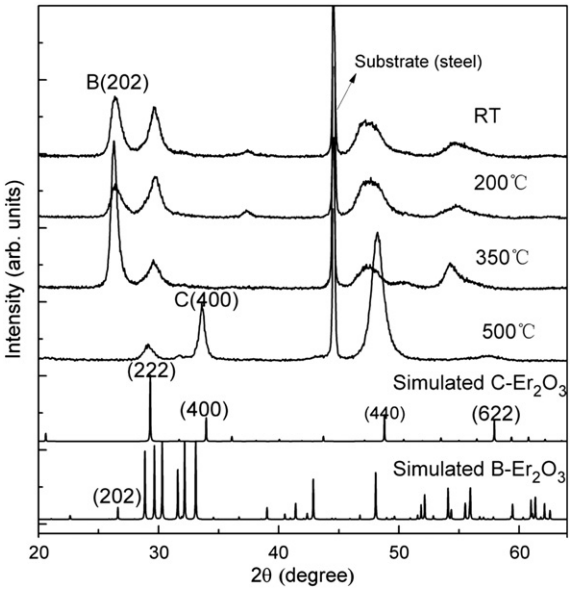

Fig. 3. XRD patterns of the Er_2O_3 coatings fabricated at different substrate temperatures. Simulated patterns of C-Er_2O_3 and B-Er_2O_3 are illustrated at the bottom.

The large position shifts of the diffraction peaks toward a low-angle direction indicate that a high compressive stress was generated during the coating growth. This stress possibly caused the B-Er_2O_3 phase formation. Guo et al. [8] reported on the phase transformation from C-Er_2O_3 to B-Er_2O_3 at RT under high pressure (9.9 GPa). Guo et al. [20] fabricated B-Er_2O_3 nanoparticles and explained that the B-Er_2O_3 formation was due to the high pressure during the particle formation that resulted from surface tension. Furthermore, the coatings fabricated by PMS in this work had high deposition rates, varying from 15 to 37 nm/min. The high deposition rates reduced the diffusion distance of the adatoms on the substrate surface and/or the growing coating surface, leading to the formation of the metastable B-Er_2O_3 phase. Adelhelm et al. [9] fabricated B-Er_2O_3 coatings using filtered cathodic arc deposition with a deposition rate of approximately 48 nm/min. They also proposed that the high deposition rate could lead to the formation of the B-Er_2O_3 phase.

Fig. 3 demonstrates the XRD patterns of the coatings deposited at RT, 200, 350, and 500 °C at 108 W. The coatings deposited at temperatures ranging from RT to 350 °C showed a monoclinic B-Er_2O_3 phase. No significant difference was observed between the patterns of coatings deposited at RT and 200 °C. However, a strong B-Er_2O_3 (202) diffraction peak was observed for the coatings deposited at 350 °C, indicating a strong [202] preferred orientation in the coating growth direction. When the substrate temperature was increased to 500 °C, the B-Er_2O_3 peaks disappeared, but the (222), (400), and (440) peaks of C-Er_2O_3 appeared. This phenomenon indicates that the coating deposited at 500 °C and 108 W possessed a cubic C-Er_2O_3 structure. During the coating deposition, a relatively low substrate temperature reduces the mobility of the adatoms on the substrate surface and/or the growing coating surface, leading to a tendency to form the metastable B-Er_2O_3 phase. By increasing the substrate temperature, the mobility of the adatoms increases, and a stable C-Er_2O_3 phase can be obtained.

The surface morphologies of the Er_2O_3 coatings were investigated using an AFM (Fig. 4). The in-plane particle sizes of the coatings increased with increasing substrate temperature. Coatings prepared at substrate temperatures from RT to 350 °C had small particles, and the average in-plane size ranged from 90 to 110 nm. As the temperature was increased to 500 °C, the small particles combined to form large particles with an average in-plane size of approximately 213 nm.

The microhardness and elastic modulus of the Er_2O_3 coatings were tested using a nanoindenter. For the coatings deposited between RT and 350 °C, the microhardness and elastic modulus of the B-Er_2O_3 coatings varied from 12.8 to 13.7 GPa and from 172 to 182 GPa, respectively. When the substrate temperature reached 500 °C, the coating structure transformed from B-Er_2O_3 to C-Er_2O_3, and the microhardness and the elastic modulus increased markedly to 16.2 and 216 GPa, respectively. The phase transformation evidently shows a remarkable effect on the hardness and elastic modulus of the coatings.

The C-Er_2O_3 coatings exhibited higher hardness and elastic modulus compared with the B-Er_2O_3 coatings. Similar results were obtained by Adehelm et al. [9]. Given that the atomic density possibly

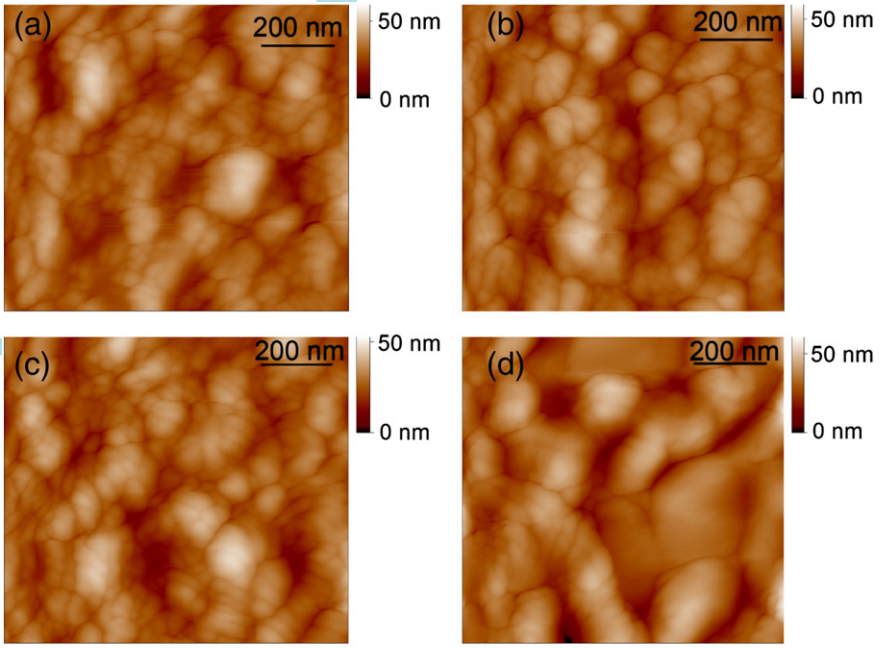

Fig. 4. AFM images (1000 nm × 1000 nm) of the coatings prepared at 108 W and at substrate temperatures of (a) RT, (b) 200, (c) 350, and (d) 500 °C.

affects the elastic modulus, the atomic densities of B-Er_2O_3 and C-Er_2O_3 were calculated. The atomic density of B-Er_2O_3 was slightly higher than that of C-Er_2O_3. However, the difference was too non-significant to affect the elastic modulus. Instead, given that elastic modulus is related to the bonding strength between atoms, the increased elastic modulus may have resulted from the changes in the bond length, bond length distribution, and crystal symmetry. A structure with high elastic modulus usually has a short average bond length and stable bond angles, conferring resistance to external forces [21]. The bond length and distribution of the two phases were analyzed statistically. Bonds with lengths beyond 3 Å were ignored due to weak interactions among atoms. Fig. 5 shows the cells of B-Er_2O_3 and C-Er_2O_3. Statistical analysis shows that the bond length of B-Er_2O_3 and C-Er_2O_3 varied from 2.172 to 2.701 Å and from 2.234 to 2.322 Å, respectively. The average bond lengths of B-Er_2O_3 and C-Er_2O_3 were 2.337 and 2.271 Å, respectively. C-Er_2O_3 had a narrower bond length distribution and a shorter average bond length compared with B-Er_2O_3. A narrow bond length distribution implies the relatively homogeneous distribution of the interatomic force in the lattice. A short average bond length implies strong atomic interactions. As a result, the C-Er_2O_3 coating had a larger elastic modulus compared with the B-Er_2O_3 coating.

Hardness is associated with the ability of a material to resist plastic deformation. This property is influenced by factors more complex than those that influence elastic modulus. However, in general, hardness is closely related to elastic modulus and both properties exhibit similar trends [22]. Therefore, this relation may also explain why the C-Er_2O_3 coating had higher microhardness relative to the B-Er_2O_3 one.

3.2. Annealing

The coatings were heat-treated to investigate their thermal stability. After annealing, no obvious pits or cracks were observed on the coating surfaces. The XRD patterns of the as-deposited and annealed

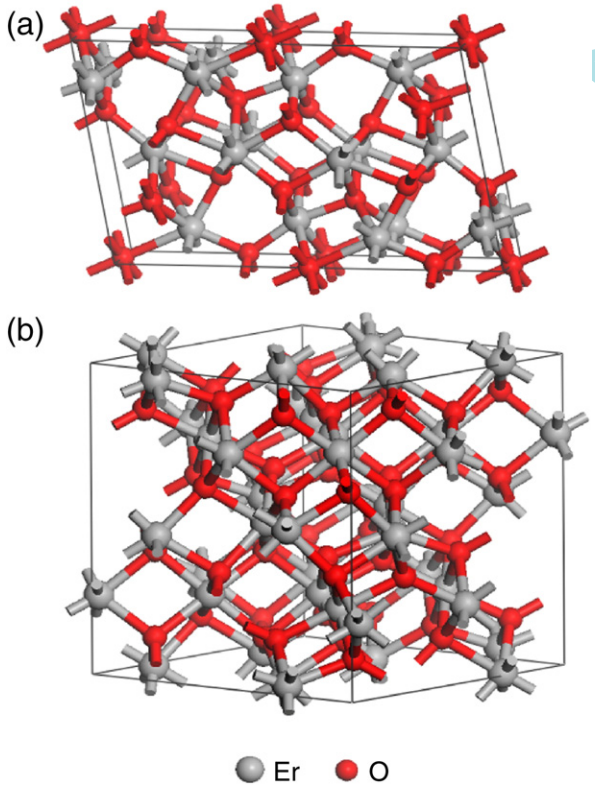

Fig. 5. The cells of (a) B-Er_2O_3 and (b) C-Er_2O_3.

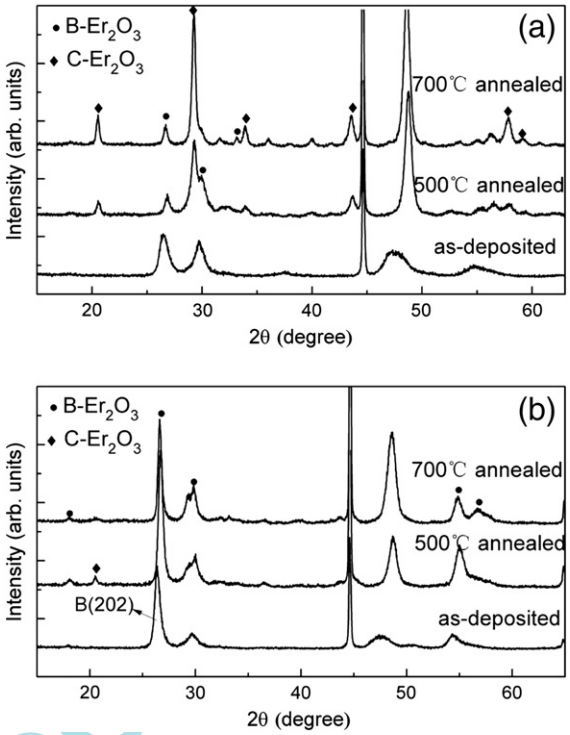

Fig. 6. XRD patterns of the as-deposited and annealed Er_2O_3 coatings deposited at (a) RT and (b) 350 °C.

Er_2O_3 coatings are shown in Fig. 6. For the coating deposited at RT, strong C-Er_2O_3 peaks and very weak B-Er_2O_3 peaks were observed after annealing. For the coating deposited at 350 °C, however, B-Er_2O_3 diffraction peaks remained strong after 700 °C annealing. The B-Er_2O_3 phase in the coating deposited at 350 °C showed a higher thermal stability than that deposited at RT. For the coatings deposited at RT and 350 °C, 2θ of B-Er_2O_3(202) shifted by only 0.08° and 0.15° toward a low-angle direction, relative to the simulated patterns after annealing at 700 °C. The reduced shifts indicate that annealing released the stress in the coatings. Furthermore, after annealing, the stress in the coating deposited at RT was smaller than that in the coating prepared at 350 °C. Adelhelm et al. [9] prepared B-Er_2O_3 coatings at RT and 400 °C, and then annealed them at 600 °C. They found that the B-Er_2O_3 coatings deposited at RT were transformed to C-Er_2O_3, whereas the coatings deposited at 400 °C retained the B-Er_2O_3 structure. They proposed that the different phase stabilities were due to the different thermal stresses induced during annealing. In the present work, the reason for the better phase stability of the B-Er_2O_3 coating deposited at high substrate temperature remains unclear. Hence, further study is necessary.

The microhardness and elastic modulus of the annealed coatings were tested. After annealing at 500 and 700 °C, the microhardness of the B-Er_2O_3 coatings deposited at 350 °C increased from 12.8 to 12.9 and 14.5 Gpa, and the elastic modulus increased from 182 to 204 and 239 Gpa, respectively. After annealing, parts of the B-Er_2O_3 phase in the coatings were transformed to the C-Er_2O_3 phase. The annealed coatings had higher microhardness and elastic modulus than the as-deposited ones because the C-Er_2O_3 coatings had higher microhardness and elastic modulus than the B-Er_2O_3 coatings.

4. Conclusions

Er_2O_3 coatings were fabricated by mid-frequency pulsed reactive magnetron sputtering at different sputtering powers and substrate temperatures. The monoclinic phase (B-Er_2O_3) was observed in the Er_2O_3 coatings prepared at substrate temperatures below 350 °C.

The cubic phase (C-Er_2O_3) was obtained by elevating the substrate temperature to 500 °C. Statistics show that C-Er_2O_3 had a narrower bond length distribution and a shorter average bond length compared with B-Er_2O_3, which may explain the increased hardness and elastic modulus of C-Er_2O_3 coatings. The annealing process induced the phase transformation from B-Er_2O_3 to C-Er_2O_3. During annealing, the B-Er_2O_3 coatings deposited at elevated substrate temperatures showed high phase stability.

Acknowledgements

The authors would like to thank the National Natural Science Foundation of China for their financial support (No. 50776010).

References

[1] Y.Y. Zhu, R. Xu, S. Chen, Z.B. Fang, F. Xue, Y.L. Fan, X.J. Yang, Z.M. Jiang, Thin Solid Films 508 (2006) 86.
[2] M. Losurdo, M.M. Giangregorio, G. Bruno, D. Yang, E.A. Irene, A.A. Suvorova, M. Saunders, Appl. Phys. Lett. 91 (2007) 091914.
[3] M.F. Al-Kuhaili, S.M.A. Durrani, Thin Solid Films 515 (2007) 2885.
[4] A. Sawada, A. Suzuki, H. Maier, F. Koch, T. Terai, T. Muroga, Fusion Eng. Des. 75 (2005) 737.
[5] D. Levchuk, S. Levchuk, H. Maier, H. Bolt, A. Suzuki, J. Nucl. Mater. 367 (2007) 1033.
[6] M. Tang, P. Lu, J.A. Valdez, K.E. Sickafus, J. Appl. Phys. 99 (2006) 063514.
[7] G. Adachi, N. Imanaka, Chem. Rev. 98 (1998) 1479.
[8] Q. Guo, Y. Zhao, C. Jiang, W.L. Mao, Z. Wang, J. Zhang, Y. Wang, Inorg. Chem. 46 (2007) 6164.
[9] C. Adelhelm, T. Pickert, M. Balden, M. Rasinski, T. Plocinski, C. Ziebert, F. Koch, H. Maier, Scr. Mater. 61 (2009) 789.
[10] F. Koch, R. Brill, H. Maier, D. Levchuk, A. Suzuki, T. Muroga, H. Bolt, J. Nucl. Mater. 329 (2004) 1403.
[11] J. Musil, P. Baroch, J. Vlcek, K.H. Nam, J.G. Han, Thin Solid Films 475 (2005) 208.
[12] P.J. Kelly, J. Hisek, Y. Zhou, R.D. Pilkington, R.D. Arnell, Surf. Eng. 20 (2004) 157.
[13] C.P.C. Wong, J.F. Salavy, Y. Kim, I. Kirillov, E. Rajendra Kumar, N.B. Morley, S. Tanaka, Y.C. Wu, Fusion Eng. Des. 83 (2008) 850.
[14] XPSPeak4.1 program. Available online, http://www.phy.cuhk.edu.hk/~surface/XPSPEAK/.
[15] N. Guerfi, O. Bourbia, S. Achour, Mater. Sci. Forum 480 (2005) 193.
[16] M.P. Singh, T. Shripathi, K. Shalini, S.A. Shivashankar, Mater. Chem. Phys. 105 (2007) 433.
[17] W. Kraus, G. Nolze, Powdercell of windows version 2.3, Available online, http://www.bam.de/de/service/publikationen/powder_cell.htm.
[18] B. Wu, M. Zinkevich, F. Aldinger, D.Z. Wen, L. Chen, J. Solid State Chem. 180 (2007) 3280.
[19] J. Wontcheu, T. Schleid, Z. Anorg. Allg. Chem. 634 (2008) 2091.
[20] B. Guo, A.S. Harvey, J. Neil, I.M. Kennedy, A. Navroteky, S.H. Risbud, J. Am. Ceram. Soc. 90 (2007) 3683.
[21] P. Ravindran, L. Fast, P.A. Korzhavyi, B. Johansson, J. Wills, O. Eriksson, J. Appl. Phys. 84 (1998) 4891.
[22] K. Bobzin, E. Lugscheider, M. Maes, C. Piaro, Thin Solid Films 494 (2006) 255.